

Title here

Elio Campitelli * and Leandro Díaz

CIMA UBA blablabla

Carolina Vera

⁵ **Corresponding author:* Elio Campitelli, elio.campitelli@cima.fcen.uba.ar

ABSTRACT

6 Enter the text of your abstract here. This is a sample American Meteorological Society (AMS)
7 \LaTeX template. This document provides authors with instructions on the use of the AMS \LaTeX tem-
8 plate. Authors should refer to the file `amspaper.tex` to review the actual \LaTeX code used to create
9 this document. The `template.tex` file should be modified by authors for their own manuscript.

10 *Significance statement.* This is significant because I wrote it.

11 **1. Introduction**

12 yada yada SAM yada yada circulation.. yada yada so important. yada yada many impacts.

13 Fogt et al. (2012) studied the characteristics of the asymmetric structure of the SAM. It computed
14 the zonally anomalous component of mean sea level pressure (MSLP) composites for positive and
15 negative SAM events and created two indices by projecting MSLP fields onto them. However,
16 the use of composites leads to some issues that affect the interpretability of the results. First, they
17 can be dependent on the choice of threshold used to define positive and negative events. Secondly,
18 by discarding data that don't meet the threshold, they don't use all the information available. Due to
19 the relatively short timeframe used, this leads to some composites being composed of as little as 4
20 years. Third, the resulting composites corresponding to each polarity and season are derived from
21 the average of different amounts of fields and from different years. This last issue is particularly
22 important in light of the changing structure of the SAM before and after 1980 (Silvestri and Vera
23 2009). In Fogt et al. (2012), the DJF SAM+ composite uses only 7 years, 5 of which are later than
24 1988, whereas all of the 8 years used for their DJF SAM- composite are from earlier than 1988.

25 **2. Methods**

26 **1) DEFINITION OF INDICES**

27 We defined the Southern Annular Mode (SAM) as the leading EOF of the monthly anomalies of
28 geopotential field at 700 hPa south of 20°S (citation?). The EOF was performed by computing the
29 Singular Value Decomposition of the data matrix consisting in 481 rows and 4176 columns (144
30 points of longitude and 29 points of latitude). The values were weighted by the square root of the

31 cosine of latitude to account for the non-equal area of each gridpoint (Chung and Nigam 1999).
32 This same method was used at the rest of the levels considered in this paper.

33 To separate between the zonally symmetric and asymmetric components of the SAM, we com-
34 puted the zonal mean and anomalies of the full SAM spatial pattern. The results are shown in
35 Figure 1 for 700hPa. The full spatial signal ($\text{EOF}_1(\lambda, \phi)$) is the sum of the zonally asymmetric
36 ($\text{EOF}_1^*(\lambda, \phi)$) and symmetric ($[\text{EOF}_1](\lambda, \phi)$) components. We then compute the “Full”, “Asym-
37 metric” and “Symmetric” indices, by regressing each geopotential field on these patterns (weighting
38 by the cosine of latitude).

39 The three indices are normalised by dividing them by the standard deviation of the “Full” index
40 at each level. This means that comparing the magnitude between indices is meaningful, but it also
41 means that not every index will have unit standard deviation.

42 2) DATA

43 We used monthly geopotential height at 2.5 longitude by 2.5 latitude resolution from ERA5
44 (Hersbach et al. 2020) for the period 1979 to 2018.

45 Monthly temperature NOAA Global Surface Temperature (NOAAGlobalTemp) 5.0 degree lati-
46 tude x 5.0 degree longitude global grid (Vose et al. 2012; Smith et al. 2008). The same analysis
47 was carried out using CRUTEM4 (Osborn and Jones 2014) (not shown).

48 We used monthly precipitation data from CPC Merged Analysis of Precipitation (Xie and Arkin
49 1997) 2.5 degree latitude x 2.5 degree longitude. CPCC: [schneider2015] #FIXME

50 3) REGRESSIONS

51 Explain multiple regression interpretation #FIXME.

52 We adjusted p-values for False Detection Rate following Wilks (2016).

3. Results

a. Temporal evolution

Figure 2 shows the Asymmetric and Symmetric time series corresponding to 700 and 50hPa. At first glance the series can be distinguished by their distributions. Whereas the tropospheric indices are approximately normally distributed, the stratospheric indices are more long-tailed; that is, extreme values (both negative and positive) abound. The Asymmetric series have both more variability in the higher frequencies than the Symmetric series.

The stratospheric Symmetric SAM varies strongly with a two-year period, which can be seen using spectral methods (Figure A3) or in the autocorrelation structure (Figure A4). There is a local peak at 2 years in the periodogram of the tropospheric Symmetric SAM also, although it's not statistically significant. In the troposphere the most significant peak of variability is found in the Asymmetric index at around 3.6 months.

From Figure 2 we can see that the Asymmetric and Symmetric time series appear to be correlated. Moreover, looking at the extremes in the stratosphere, the Symmetric series appears to lag the Asymmetric series (see, for example, the positive events on late 1987 marked with a circle). We show these correlations, across all the levels of the reanalysis and for zero and -1 lag (Asymmetric index leading the Symmetric index), in Figure 3.

Zero-lag correlations between the Asymmetric and Symmetric series are relatively constant throughout the troposphere, fluctuating between 0.39 and 0.45. One-month-lag correlations are similarly constant but significantly reduced, hovering around 0.17. In the stratosphere, zero-lag correlations drop to a minimum of 0.21 at 20 hPa and then it increases again monotonically with height up to the uppermost level of the reanalysis. At the same time, one-month-lag correlations increase with height.

Figure 4a) shows (zero-lag) cross-correlation across levels for the Full, Symmetric and Asymmetric SAM indices. For the Full SAM (panel a), high values below 100 hPa reflect the vertical (zero-lag) coherency throughout the troposphere. Above 100 hPa correlation between levels falls off more rapidly, indicating less coherent (zero-lag) variability. Still there is a non negligible correlation between the troposphere and the lower-to-middle stratosphere. Examining panels b and c, we see that the Asymmetric and Symmetric SAM share the same high level of coherency in the troposphere but they differ in their stratospheric behaviour. As evidenced by the wider dark red areas near the diagonal in Figure 4b) vs. Figure 4c), stratospheric coherency is stronger for the Asymmetric SAM than the Symmetric SAM. The stratospheric Symmetric SAM seems to connect more strongly to the troposphere than the Asymmetric SAM; this can be seen by the lower correlation values in the top right left of Figure 4b) in comparison with Figure 4c).

Figure 5 shows normalised decadal trends for each index for the whole period 1979-2018 along with the 95% confidence interval in shading for the whole year (row a) and separated by trimesters (rows b through e). As previously documented (e.g. Fogt and Marshall (2020)), there is a statistically significant increase towards more positive SAM (panel a.1), which is evident only in Summer and Autumn (panels b.1 and c.1). We observe these increases mainly in the troposphere, reaching their maximum at 100 hPa in Summer. By separating the SAM signal in its Asymmetric and Symmetric parts, we can not only see that these trends are almost entirely due to the Symmetric component (columns 2 vs. columns 3), but in some cases the trends become more clear. In Summer, the Asymmetric SAM has a statistically non significant negative trend in the middle troposphere that obscures the signal; as a result, trends computed using only the Symmetric component are more clear (compare the shading region in panel b.1 and b.3). In Autumn, using the Symmetric SAM reveals a statistically significant positive trend in the stratosphere that is not significant using the Full index.

We stress that these are only linear trends during the whole period and the absence of a statistically significant signal should not be taken as evidence of no systematic change. In particular, going back to Figure 2, we can see an evident change in the stratospheric Asymmetric component (red line in panel a) between the 90's, when we see a dominance of extreme negative values, and the 00's, when we see the inverse. This change is restricted to the Winter months: the linear trend for JJA starting in 1990 for the Asymmetric component at 50hPa is 0.37 ± 0.22 .

Figure 6 shows decadal trends for the explained variance of each index. There is no evidence of a significant trend in the stratosphere. In the troposphere, there is a positive trend for the Asymmetric SAM and no significant trend for the Symmetric SAM. This suggests that the SAM has become more asymmetric in the period from 1979 to 2018. The change is slight, though; of the order of 1% increased explained variance per decade.

b. Spatial patterns

To show if, and to what extent, the Asymmetric and Symmetric SAM indices indeed capture the asymmetric and symmetric component of the SAM respectively, we computed the spatial regression of geopotential height anomalies on these indices and the Full SAM index. Figure 7 shows these regressions. Regression coefficients in column a are computed using the Full SAM. Regression coefficients in columns b and c are computed using multiple regression using the Asymmetric and Symmetric indices at the same time. Thus, they are to be interpreted as the patterns associated with each index, removing the variability (linearly) explained by the other index.

In the stratosphere, the spatial pattern associated with the Full SAM is more clearly dominated by a zonally symmetric, monopolar structure (panel a.1) which is, however, not perfectly centered in the south pole. The monopole obtained by multiple regression with the Asymmetric and Symmetric

123 SAM (panel c.1) is much more symmetric and the shift from total symmetry is captured by the
124 regression pattern of the Asymmetric SAM as a wave-1 with maximum anomalies above the
125 Belinghausen Sea on the Western Hemisphere and Davids Sea in the Eastern Hemisphere
126 (panel b.1).

127 In the troposphere, panel a.2 shows the well known zonally symmetrical annular mode *contami-*
128 *nated* with zonal asymmetries in the form of a wave-3. The regression using the Asymmetric and
129 Symmetric SAM indices successfully disentangle both structures. The Asymmetric component
130 gives rise to a cleaner zonal wave (panel b.2) and the Symmetric component is associated with an
131 trully annular mode, almost devoid of zonal asymmetries (panel c.2). The wave-3 pattern observed
132 in panel b.2 is rotated by half a wavelength from the average position of the mean wave-3 pattern
133 asociated with Raphael (2004)'s ZW3 index, whose reference locations are marked with points in
134 the figure. Thus, the tropospheric Asymmetric SAM index responds to zonal displacements in the
135 position of the wave-3 pattern.

136 The amplitude of each zonal wave number at each latitude at 50 hPa and 700 hPa is shown
137 in Figure 8, where wave number zero represents the amplitude of the zonal mean. Comparing
138 between rows, this Figure quantifies the relatively clean separation between the zonally symmetric
139 and zonally asymmetric structures, as its evident how the mixture of waves of the Full field (column
140 a) is very similar to the sum of the waves of the Asymmetric and Symmetric field (columns b and c,
141 respectively). Column b of Figure 8 shows that the Asymmetric SAM is overwhelmingly dominated
142 by wave 1 in the stratosphere (panel b.1), while in the troposphere it is composed of zonal waves 3
143 to 1 in decreasing level of importance (panel b.2).

144 To analyse the vertical structure of the geopotential anomalies asociated with the asymmetric SAM
145 index, we show a vertical cross section of regressions of mean geopotential height between 651S

146 and 40% for the 50 hPa Asymmetric SAM index (panel a) and for the 700 hPa Asymmetric SAM
147 index (panel b) (Figure 9).

148 The geopotential anomalies associated with the stratospheric SAM (panel a) are clearly con-
149 strained to the stratosphere, which underscores the disconnect between the stratospheric and tro-
150 pospheric Asymmetric SAM. The vertical structure this signal tilts about 60% to the West between
151 100 hPa and 1 hPa, suggesting baroclinic processes and polarward transport of heat (#FIXME is
152 this ok?). Interestingly, the signal in the stratosphere maximises near 10 hPa despite using the 50
153 hPa index for the regression.

154 The tropospheric Asymmetric SAM (panel b) has significant signals that extend upwards to the
155 uppermost levels of the reanalysis. In the troposphere, the wave-3 structure is equivalent barotropic
156 with maximum amplitude at roughly 250 hPa. The anomalies are much more intense in the Western
157 hemisphere, where they extent into the stratosphere. In the Eastern hemisphere the wave-3 signal
158 is weaker and confined to the troosphere while negative anomalies dominate in the stratosphere.
159 So, while the tropospheric Asymmetric SAM index is associated with stratospheric geopotential
160 anomalies, these do not project strongly onto the stratospheric Asymmetric SAM.

161 The structures shown in panels a and b in Figure 9 are surprisignly robust to the choice of index
162 level. For any stratospheric (above 100 hPa) index, the resulting anomalies are very similar to the
163 wave-1 structure with maximum near 10 hPa in panel a. Conversely, for any tropospheric (below
164 100 hPa) index, the result is very similar to panel b. Pattern cross-correlation is greater than 0.9
165 within stratospheric index levels and tropospheric index levels and less than .4 accross stratospheric
166 and tropospheric levels (Figure A8), i.e. regressions obtained using Asymmetric SAM indices in
167 the troposphere are very similar to each other and different to the ones obtaines using indices in the
168 stratosphere and vice versa. The patterns mainly change in amplitude. The tropospheric pattern

is maximised by the 300 hPa Asymmetric SAM index and the stratospheric pattern increased monotonically with height.

The wave-3 pattern from Figure 7 panel b.2 is very similar to the teleconnection pattern associated with the ENSO. Indeed, Fogt et al. (2011) showed that there is a significant relationship between the SAM and the ENSO. The correlation between the full SAM and the ENSO as measured by the Multivariate Enso Index (Wolter and Timlin 2011) is -0.19. This relationship is captured entirely the Asymmetric SAM, as this index has a partial correlation of -0.27 with the MEI, whereas the Symmetric SAM's partial correlation with the MEI is essentially null (-7.9×10^{-4}).

c. Impacts

1) TEMPERATURE

Figure 10 shows regression coefficients of each index at 700 hPa with surface temperature for each trimester. It is evident that the Asymmetric and Symmetric SAM indices are associated with overall distinct temperature patterns which can be obscured when using the Full SAM index. The Symmetric SAM signal is weaker than the Asymmetric SAM, as evidenced by the relatively smaller and less statistically significant regression coefficients in row 3 of Figure 10 compared with row 2.

In DJF (row 1), the strong negative signal in the tropical Pacific in panel a.1 is mostly associated with the Asymmetric component (panel b.1), as is it largely absent in the Symmetric component (panel c.1). Furthermore, the Asymmetric SAM is also associated with low temperature anomalies in the Indian ocean, but this signal is obscured by the Symmetric variability and thus lost in the Full SAM. Over the continents, the Asymmetric SAM is associated with negative temperature anomalies which, again, mostly disappear in the Full SAM regression. Temperature regression with the Symmetric SAM (panel c.1) shows a ring of negative anomalies around Antarctica surrounded

by positive anomalies. This pattern of anomalies is consistent with thermal wind balance and the intensification and pole-ward migration of the westerlies commonly linked to the SAM.

The patterns seen in MAM and JJA (rows 2 and 3) are not robustly significant in the sense that there are no areas with p-values below 0.05 when controlling for FDR following Wilks (2016). Nevertheless, it is interesting to note that in both trimesters, the sign of the regression is consistently flipped between the Asymmetric and Symmetric regressions. In South America, for example, the Asymmetric SAM is associated with positive temperature anomalies in MAM and negative temperature anomalies in JJA, while the opposite is the case for the Symmetric SAM.

Finally, in SON (row 4) there is no significant temperature signal associated with the Symmetric SAM (panel c.4), while the Asymmetric SAM shows a relatively robust signal in the equatorial Pacific, Australia, and even Southeast South America.

2) PRECIPITATION

Regression of the SAM indices with seasonal mean precipitation are shown Figures 11 and 12 for Australia and New Zealand, and South America respectively. (We didn't detect any significant signal in South Africa.)

In Australia (Figure 11), the annual-level regression shows that the Full SAM is associated with a statistically significant increase in precipitation in the Southeastern region (panel a.1), which reproduces the results from Gillett et al. (2006). The separation between Asymmetric and Symmetric SAM suggest that this increase is explained by the Symmetric SAM only in the East coast (panel c.1), which is consistent with the increased easterly flow clearly seen in relation with this index. The Asymmetric SAM appears related to increased precipitation in the West coast of Southeastern Australia (panel b.2), explained by the anomalous *westerly* circulation transporting moist air to the continent.

214 The seasonal-level regressions show statistically significant anomalies only in SON, with a
215 pattern similar to the annual-level regression (panel a.5). Panels b.5 and c.5 don't show a clear
216 separation between the Asymmetric and Symmetric SAM. If anything, the positive and more
217 significant regression coefficients in panel b.5 vs pane c.5 would suggest more influence of the
218 Asymmetric than the Symmetric SAM, going against the interpretation gathered from the annual-
219 level regressions. This Spring signal is broadly consistent with Hendon et al. (2007), but whereas
220 Hendon et al. (2007) also detected a strong signal in Summer, panel a.2 shows no statistically
221 significant association (although the coefficients have the consistent sign).

222 In South America (Figure 12), the annual-level regression shows that the SAM is associated
223 with statistically significant precipitation decrease in Southeastern South America (SESA) and
224 Southern Chile and non-significant increase in South Brazil, near the South Atlantic Convergence
225 Zone (SACZ) (panel a.1).

226 Panels b.1 and c.1 show a remarkably clean separation between the Asymmetric SAM –associated
227 with the Southeastern South American and Southern Brazilian signals– and the Symmetric SAM
228 –associated with the signal in Southern Chile. This separation is consistent with the mechanisms
229 responsible for these effects. In Southern Chile, the reduced westerly flow reduce moisture transport
230 from the Pacific Ocean (cita?? #FIXME).

231 In Southeastern South America, anomalous meridional winds lead to less precipitation by in-
232 hibiting moisture convergence from the South American Low Level Jet (Silvestri and Vera 2009).
233 The increased precipitation in the South Atlantic Convergence Zone, on the other hand, appears to
234 be related to modulation of the anomalous SAM circulation in SACZ events which lead to more
235 frequent and intense SACZ events during positive SAM (Rosso et al. 2018).

There is a small area of increased precipitation with SAM near central Argentina which is also present in the station-based analysis by Gillett et al. (2006) and that is explained by the Asymmetric SAM.

Except during Winter, the seasonal-level regression all show these similar patterns although not as cleanly and only in some cases statistically significant.

3) SEA ICE

Regressions between the Full SAM index and Antarctic Sea Ice Concentrations (Figure 13) show a great deal of variability across seasons. The only statistically significant signal is in Spring, when we observe negative concentration anomalies in the Northern Weddell Sea (panel a.4) explained by the Asymmetric SAM (panel b.4). Both in Winter and in Spring the Asymmetric SAM is associated with bigger Sea Ice Concentration anomalies in West Antarctica than East Antarctica, with generally decreased concentration East of the Antarctic Peninsula and increased concentration to the West, as expected from the anomalous circulation correlated with this index. The Symmetric SAM signal appears more evenly distributed across the whole ice sheet.

d. Conclusions

We presented a method to systematically separate the zonally asymmetric and zonally symmetric components of the SAM into two indices. As expected, they are significantly correlated with each other, but they also have their own unique dynamics such as different vertical coherence patterns, variability and long term trends.

The spatial structure and temporal evolution of the SAM show a strong separation between the stratosphere SAMs. The first EOF in the stratosphere is monopolar in nature while the first EOF in the troposphere is a proper annular mode. Their respective departures from the zonal mean

are also different: a zonal wave 1 dominates the stratospheric SAM; waves 3 and 2 dominate the tropospheric SAM. Furthermore, there is little temporal correlation between the tropospheric and stratospheric time series.

The zonal asymmetric component of the SAM at each level is even more decoupled between the troposphere and the stratosphere. Their temporal evolution shows essentially zero correlation (Figure 4) and the signal associated with the stratospheric Asymmetric SAM is completely restricted to the stratosphere (Figure 9 panel a). Geopotential height anomalies associated with the tropospheric Asymmetric SAM, on the other hand, do extend to the stratosphere, but those anomalies do not project strongly into the stratospheric Asymmetric SAM.

We show that the observed positive trend towards positive SAM is restricted to the tropospheric SAM and is explained by the Symmetric component (Figure \ref{fig:trends}). However, the degree of asymmetry appears to have increased slightly in the last 40 years, as the Asymmetric SAM explains an increasingly proportion of the variance (Figure 6).

Temperature and precipitation anomalies associated with the SAM respond to various processes in different locations. The Asymmetric and Symmetric indices do a reasonable job separating some of them. The strong summertime temperature anomalies in the equatorial Pacific are explained by the Asymmetric component, most likely due to its relationship with ENSO. The Symmetric SAM, on the other hand, captures the change in meridional temperature gradient, which is linked to the SAM-zonal wind relationship by thermal wind balance.

The patterns of SAM-associated precipitation anomalies are similarly well separated. In South America, we show that negative anomalies observed in Chile related to the SAM are well explained by the Symmetric component, while the precipitation dipole in Southern South America and the South Atlantic Convergence Zone is explained by the Asymmetric component.

LIMITATIONS

Our method assumes linearity in the asymmetric component of the SAM. That is, assumes that zonal symmetries associated with positive SAM are opposite and equal to the ones associated with negative SAM. Fogt et al. (2012)'s composites suggest that this might not be entirely valid, although we argue that much of that apparent non-linearity is due to the heterogeneous nature of the selected years for constructing the composites. Using our data (from 1979 to 2018), seasonal composites of zonal anomalies of 700 hPa geopotential height for SAM+ and SAM- show pattern linear correlations greater than -0.7 for all seasons and are visually very linear (Figure A9). Therefore, we believe that our method is at the very least a reasonable approximation of the phenomenon.

We also assumed that the structure of the SAM zonal anomalies is stable in all seasons. Again, this is not unreasonable, as geopotential zonal anomalies computed by projecting the first EOF of *each season* are very similar to each other (Figure A10).

Silvestri and Vera (2009) showed that impacts linked to the SAM changed rather dramatically before and after 1980. In particular, the negative relationship with precipitation in South America (consistent with Figure 12 panel a.1) was absent in some areas and switched sign in other in the earlier period. The correlation between ENSO and SAM is similarly non-stationary, also disappearing before 1973.

Seeing as both the ENSO-SAM relationship and most of the precipitation impacts in South America are captured by the Asymmetric SAM, the results presented here are most likely period-dependent. Therefore, it is very likely that if we were to repeat this analysis using pre-satellite data, the resulting Asymmetric SAM would look very different.

Acknowledgments. CMAP Precipitation data provided by the NOAA/OAR/ESRL PSL, Boulder, Colorado, USA, from their Web site at <https://psl.noaa.gov/> #FIXME

304 NOAA Global Surface Temperature (NOAAGlobalTemp) data provided by the
305 NOAA/OAR/ESRL PSL, Boulder, Colorado, USA, from their Web site at <https://psl.noaa.gov/>

306 References

307 Chung, C., and S. Nigam, 1999: Weighting of geophysical data in Principal Component
308 Analysis. *Journal of Geophysical Research: Atmospheres*, **104 (D14)**, 16 925–16 928, doi:
309 10.1029/1999JD900234.

310 Fogt, R. L., D. H. Bromwich, and K. M. Hines, 2011: Understanding the SAM influ-
311 ence on the South Pacific ENSO teleconnection. *Clim Dyn*, **36 (7)**, 1555–1576, doi:
312 10.1007/s00382-010-0905-0.

313 Fogt, R. L., J. M. Jones, and J. Renwick, 2012: Seasonal Zonal Asymmetries in the Southern
314 Annular Mode and Their Impact on Regional Temperature Anomalies. *J. Climate*, **25 (18)**,
315 6253–6270, doi:10.1175/JCLI-D-11-00474.1.

316 Fogt, R. L., and G. J. Marshall, 2020: The Southern Annular Mode: Variability, trends, and
317 climate impacts across the Southern Hemisphere. *WIREs Climate Change*, **11 (4)**, e652, doi:
318 10.1002/wcc.652.

319 Gillett, N. P., T. D. Kell, and P. D. Jones, 2006: Regional climate impacts of the Southern Annular
320 Mode. *Geophysical Research Letters*, **33 (23)**, doi:10.1029/2006GL027721.

321 Hendon, H. H., D. W. J. Thompson, and M. C. Wheeler, 2007: Australian Rainfall and Surface
322 Temperature Variations Associated with the Southern Hemisphere Annular Mode. *J. Climate*,
323 **20 (11)**, 2452–2467, doi:10.1175/JCLI4134.1.

324 Hersbach, H., and Coauthors, 2020: The ERA5 global reanalysis. *Quarterly Journal of the Royal*
325 *Meteorological Society*, **146 (730)**, 1999–2049, doi:10.1002/qj.3803.

326 Osborn, T. J., and P. D. Jones, 2014: The CRUTEM4 land-surface air temperature data set:
 327 Construction, previous versions and dissemination via Google Earth. *Earth System Science*
 328 *Data*, **6** (1), 61–68, doi:10.5194/essd-6-61-2014.

329 Raphael, M. N., 2004: A zonal wave 3 index for the Southern Hemisphere. *Geophysical Research*
 330 *Letters*, **31** (23), doi:10.1029/2004GL020365.

331 Rosso, F. V., N. T. Boiaski, S. E. T. Ferraz, and T. C. Robles, 2018: Influence of the Antarctic
 332 Oscillation on the South Atlantic Convergence Zone. *Atmosphere*, **9** (11), 431, doi:10.3390/
 333 atmos9110431.

334 Silvestri, G., and C. Vera, 2009: Nonstationary Impacts of the Southern Annular Mode on Southern
 335 Hemisphere Climate. *J. Climate*, **22** (22), 6142–6148, doi:10.1175/2009JCLI3036.1.

336 Smith, T. M., R. W. Reynolds, T. C. Peterson, and J. Lawrimore, 2008: Improvements to NOAA’s
 337 Historical Merged Land–Ocean Surface Temperature Analysis (1880–2006). *J. Climate*, **21** (10),
 338 2283–2296, doi:10.1175/2007JCLI2100.1.

339 Vose, R. S., and Coauthors, 2012: NOAA’s Merged Land–Ocean Surface Temperature Analysis.
 340 *Bull. Amer. Meteor. Soc.*, **93** (11), 1677–1685, doi:10.1175/BAMS-D-11-00241.1.

341 Wilks, D. S., 2016: “The Stippling Shows Statistically Significant Grid Points”: How Research
 342 Results are Routinely Overstated and Overinterpreted, and What to Do about It. *Bull. Amer.*
 343 *Meteor. Soc.*, **97** (12), 2263–2273, doi:10.1175/BAMS-D-15-00267.1.

344 Wolter, K., and M. S. Timlin, 2011: El Niño/Southern Oscillation behaviour since 1871 as diag-
 345 nosed in an extended multivariate ENSO index (MEI.ext). *International Journal of Climatology*,
 346 **31** (7), 1074–1087, doi:10.1002/joc.2336.

347 Xie, P., and P. A. Arkin, 1997: Global Precipitation: A 17-Year Monthly Analysis Based on
348 Gauge Observations, Satellite Estimates, and Numerical Model Outputs. *Bull. Amer. Meteor.*
349 *Soc.*, **78 (11)**, 2539–2558, doi:10.1175/1520-0477(1997)078<2539:GPAYMA>2.0.CO;2.

APPENDIX

Extra figures

352	LIST OF FIGURES	
353	Fig. 1. Spatial patterns of the first EOF of 700 hPa geopotential height	21
354	Fig. 2. Time series for the asymmetric SAM and symmetric SAM and density estimates	22
355	Fig. 3. Correlation between the Symmetric and Asymmetric SAM at each level for lag zero and lag	
356	-1 (Asymmetric leads Symmetric)	23
357	Fig. 4. Cross correlation between levels of the Full, Asymmetric and Symmetric SAM	24
358	Fig. 5. Decadal normalised trends for each index at each level for annual (row a) and seasonal values	
359	(rows b-e) for the period 1979-2018	25
360	Fig. 6. Decadal trends for explained variance of each index at each level for the period 1979-2018	26
361	Fig. 7. Regression patterns of geopotential height at 30, 300 and 700 hPa with the Full, Asymmetric	
362	and Symmetric SAM	27
363	Fig. 8. Planetary wave amplitude for the regression patterns at 50 and 700 hPa	28
364	Fig. 9. Asymmetric coefficient of the multiple regression of mean monthly geopotential height	
365	anomalies between 65 and 40 South	29
366	Fig. 10. Regression pattern of surface temperature with Asymmetric and Symmetric SAM	30
367	Fig. 11. Regression pattern of precipitation with Asymmetric and Symmetric SAM	31
368	Fig. 12. Same but for america	32
369	Fig. 13. Seasonal regression of SAM indices with sea ice concentration	33
370	Fig. A1. Lag-correlation between Symmetric and Asymmetric SAM at each level.	34
371	Fig. 14. Cross-correlation functions for each index and two different base levels	35
372	Fig. A3. Fourier spectrum of each timeseries. The shading indicates the 95% area derived by fitting	
373	an AR process to each series and bootstrapping 5000 simulated samples.	36
374	Fig. A4. Autocorrelation functions of each timeseries	37
375	Fig. A8. Pattern cross-correlation #FIXME!	38
376	Fig. 15. 700 hPa Geopotential height zonal anomalies of composites of positive and negative SAM	
377	months selected using 1 standard deviation as threshold	39
378	Fig. 16. Zonal projection of 700 hPa onto the first EOF of each season	40

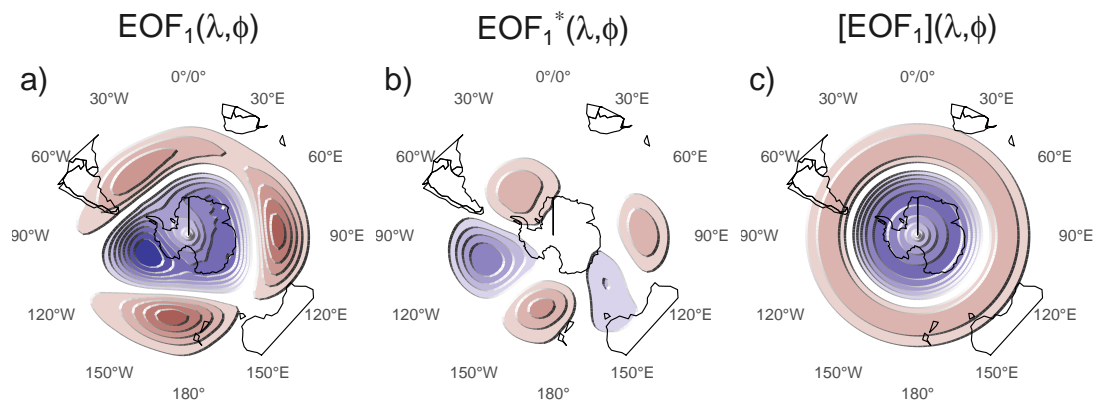


FIG. 1: Spatial patterns of the first EOF of 700 hPa geopotential height. Full field (left), zonally asymmetric component (middle) and zonally symmetric component (right). Arbitrary units.
fig:method

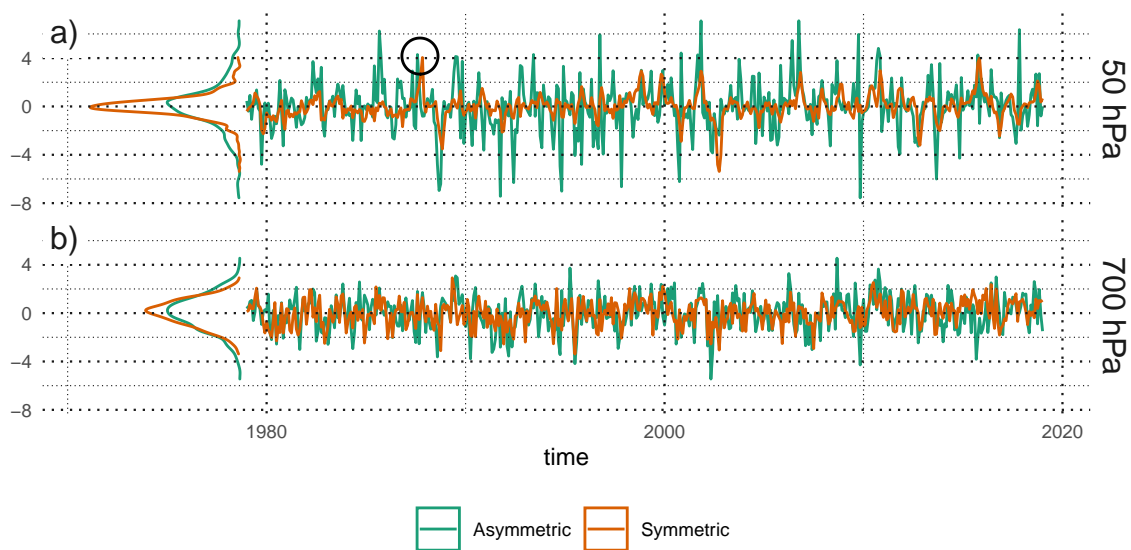


FIG. 2: Time series for the asymmetric SAM and symmetric SAM and density estimates.
fig:asysam-timeseries

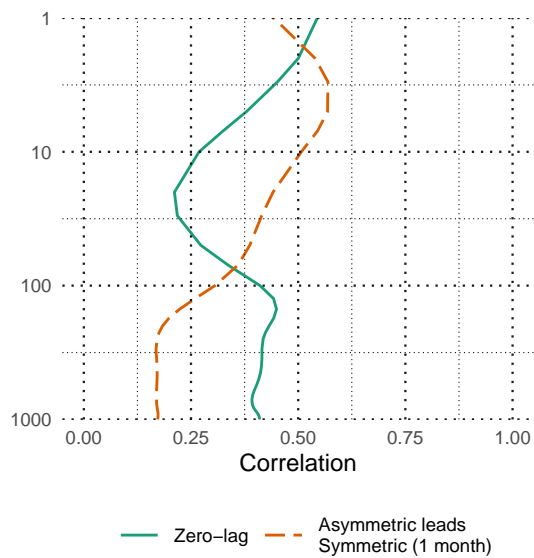


FIG. 3: Correlation between the Symmetric and Asymmetric SAM at each level for lag zero and lag -1 (Asymmetric leads Symmetric).

fig:cor-lev

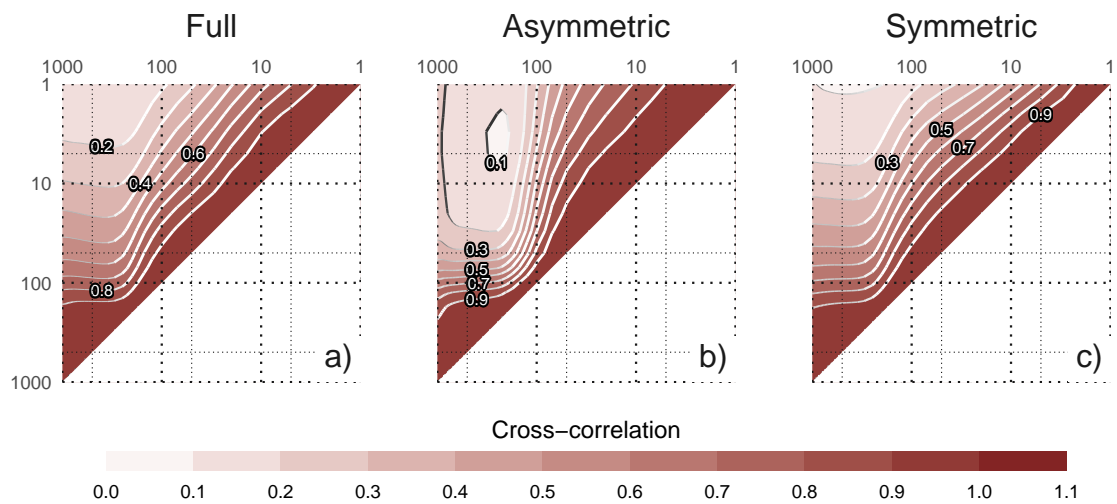


FIG. 4: Cross correlation between levels of the Full, Asymmetric and Symmetric SAM.
fig:cross-correlation

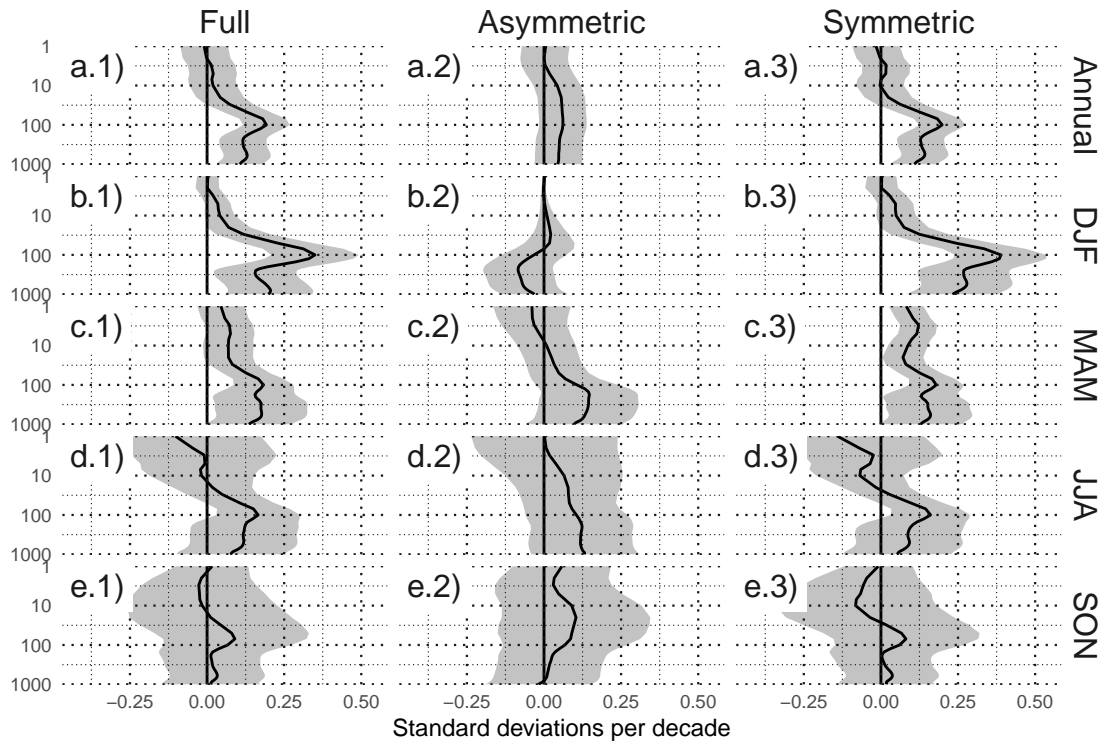


FIG. 5: Decadal normalised trends for each index at each level for annual (row a) and seasonal values (rows b-e) for the period 1979-2018. Shading indicates the 95% confidence interval.

fig:trends

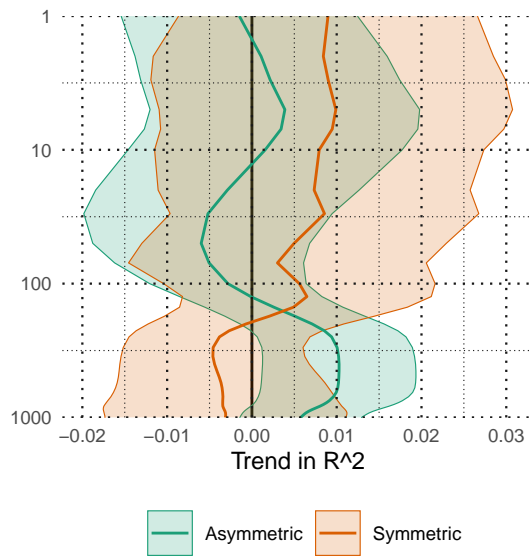


FIG. 6: Decadal trends for explained variance of each index at each level for the period 1979-2018. Shading indicates the 95% confidence interval.

fig:r-squared-trend

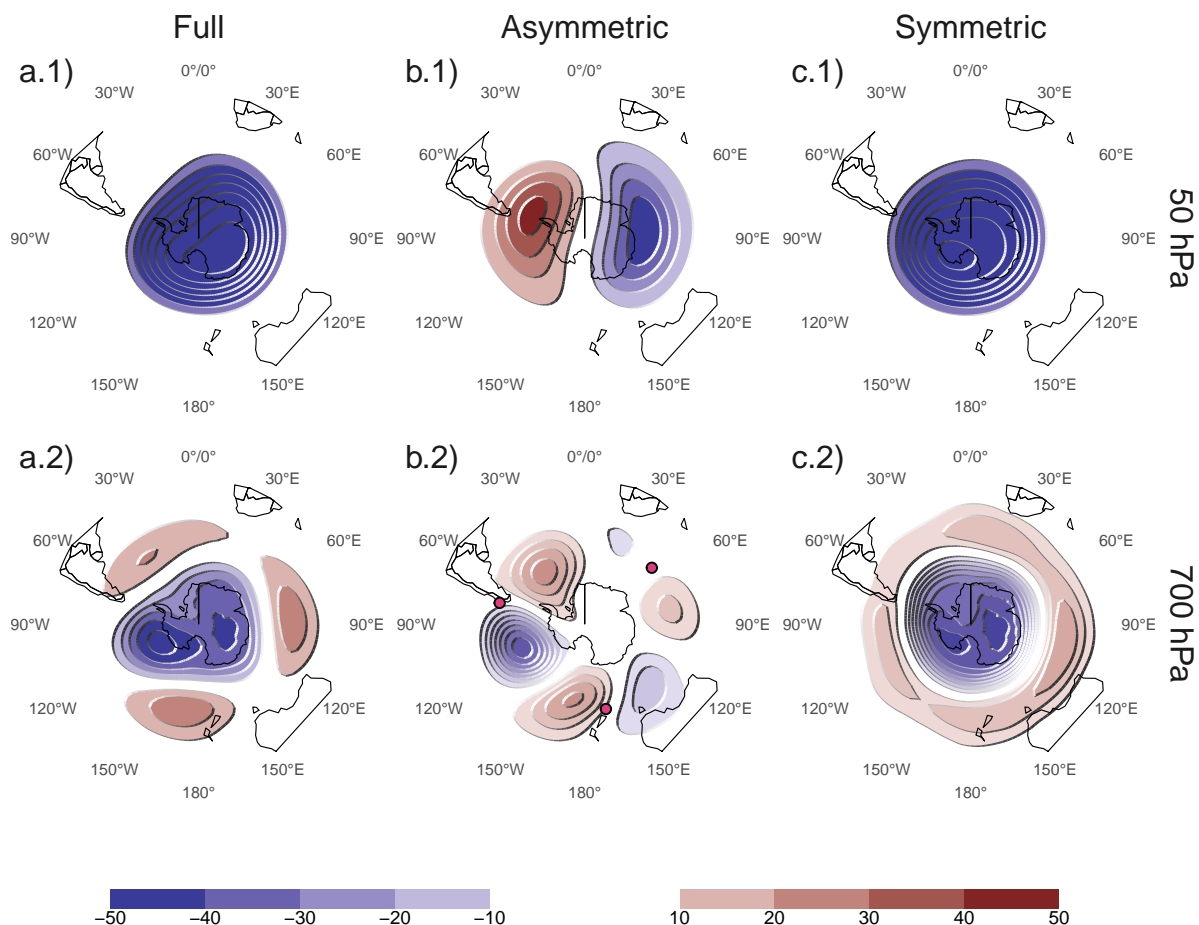


FIG. 7: Regression patterns of geopotential height at 30, 300 and 700 hPa with the Full, Asymmetric and Symmetric SAM. The regression patterns for Asymmetric and Symmetric SAM are the result of one multiple regression using both indices, not of two simple regressions involving each index by itself. Points marked on panel b.2 are the location of the reference points used by Raphael (2004) for its Zonal Wave 3 index.

fig:2d-regr

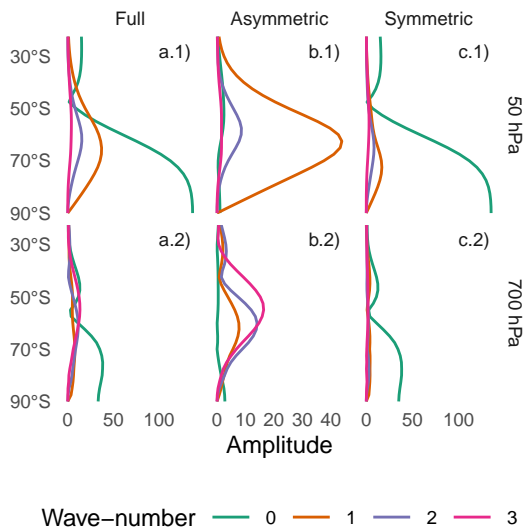


FIG. 8: Planetary wave amplitude for the regression patterns at 50 and 700 hPa. Note the varying x axis.

fig:wave-amplitude

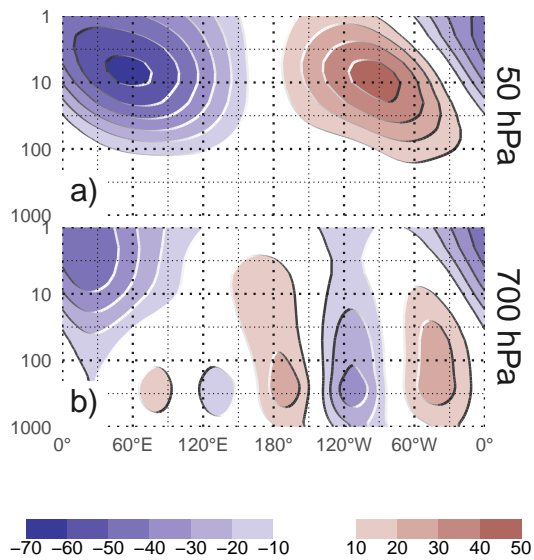


FIG. 9: Asymmetric coefficient of the multiple regression of mean monthly geopotential height anomalies between 65 and 40 South. (#FIXME this caption needs some love)
fig:vertical-regression

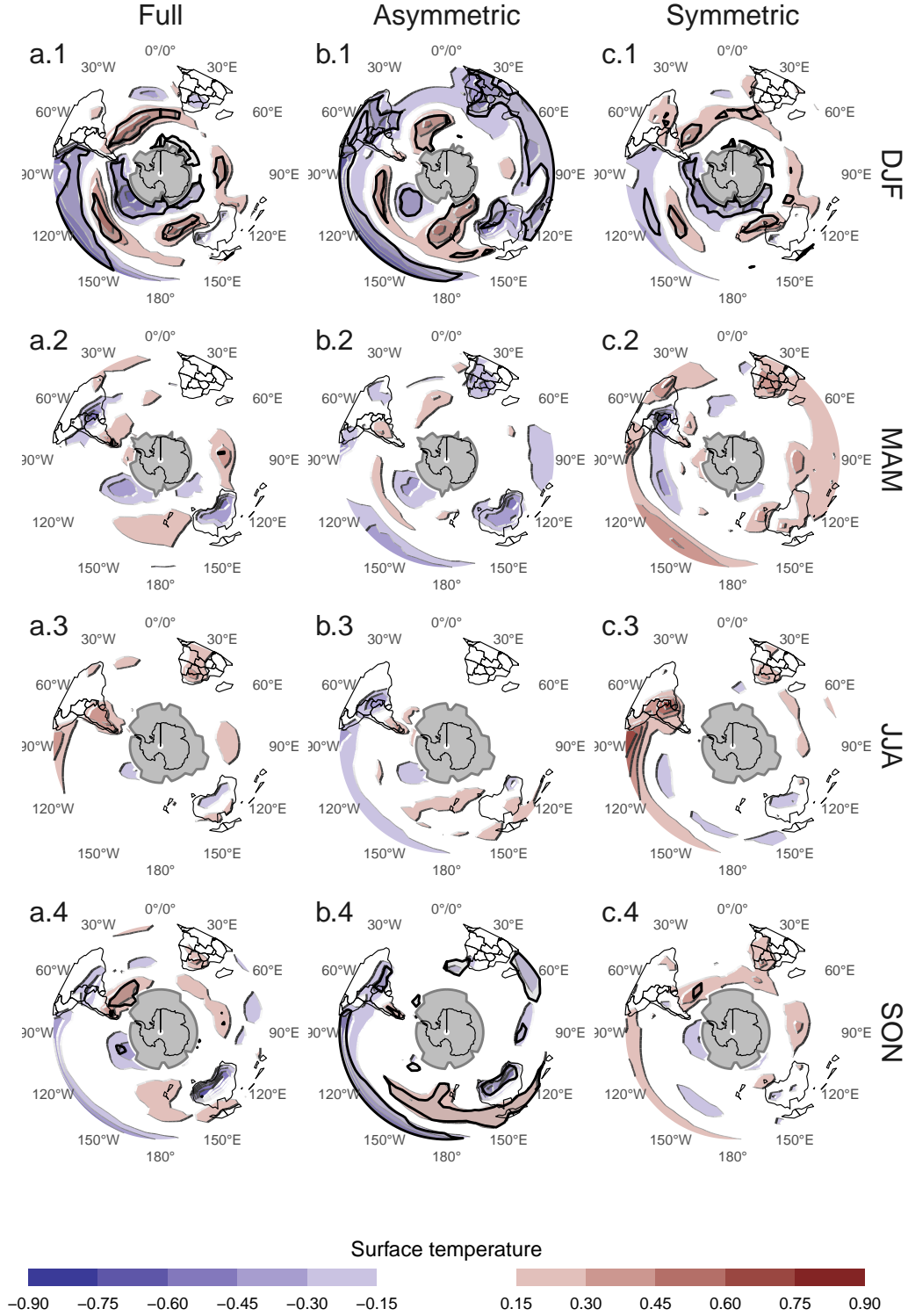


FIG. 10: Regression pattern of surface temperature with Asymmetric and Symmetric SAM. P-values smaller than 0.05 (controlling for False Detection Rate) as hatched areas. Gray areas have more than 15% of missing data.

fig:regr-air-season

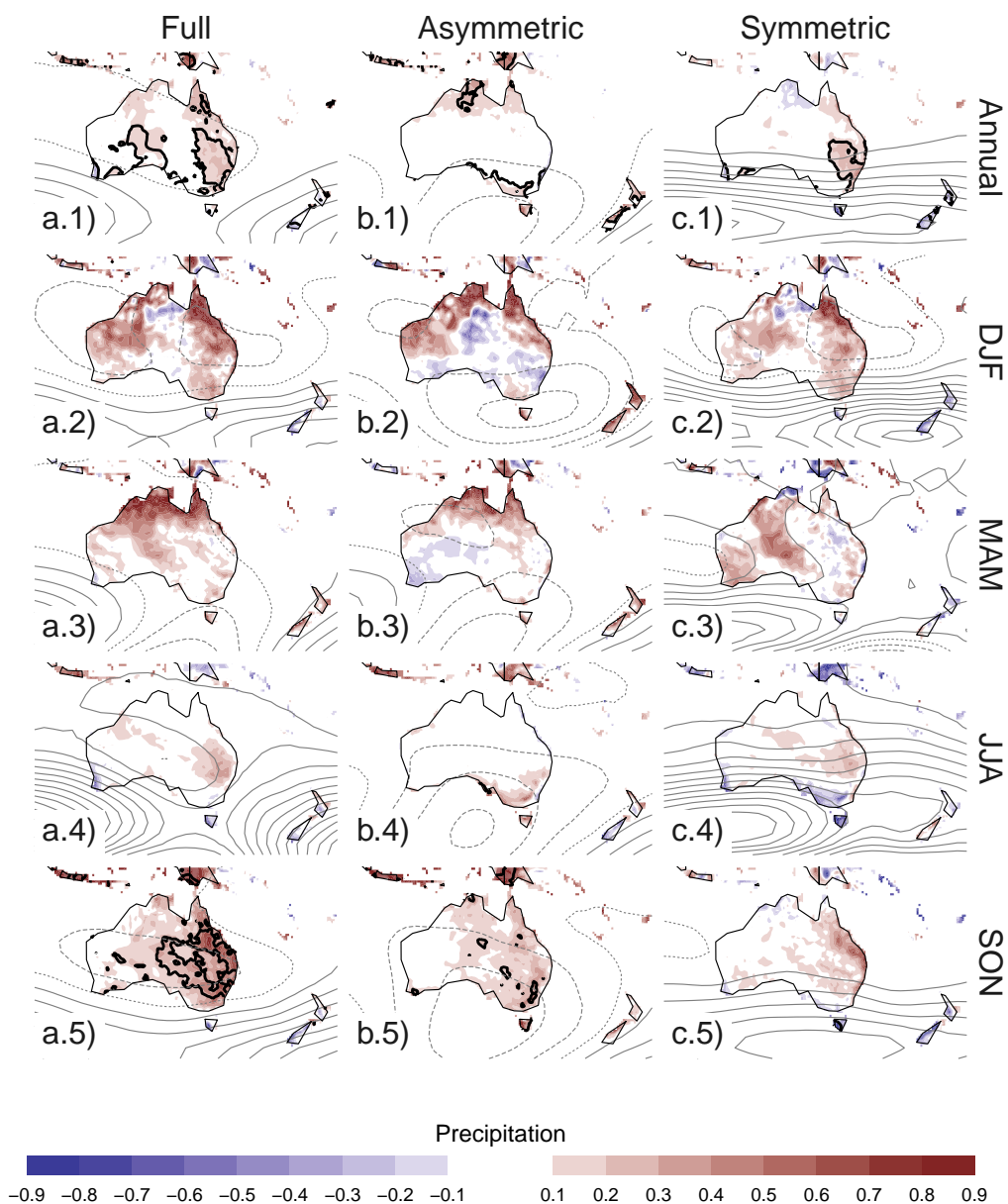


FIG. 11: Regression pattern of precipitation with Asymmetric and Symmetric SAM. P-values smaller than 0.05 (controlling for False Detection Rate) as hatched areas.

fig:pp-regr-oceania

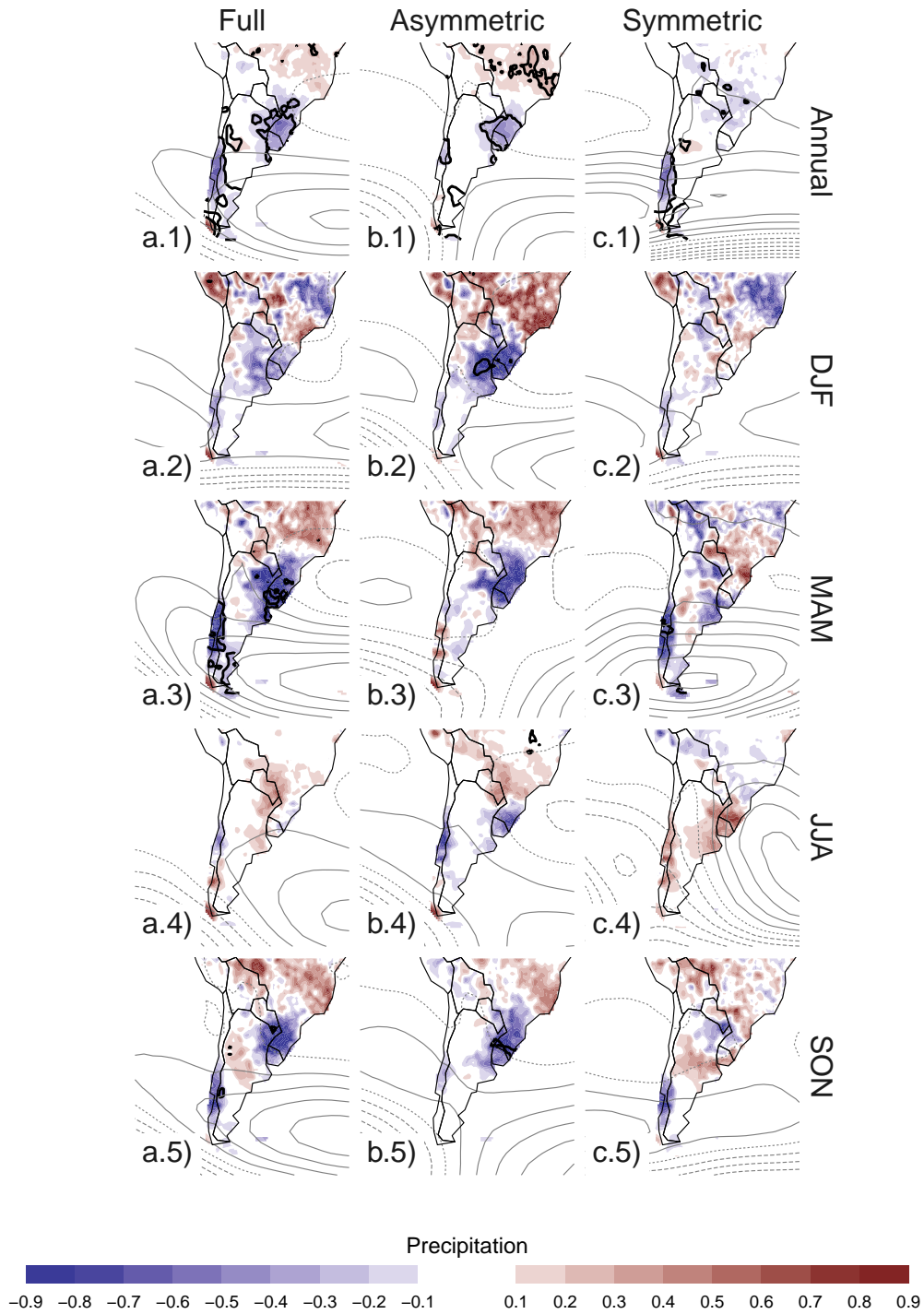


FIG. 12: Same but for america

fig:pp-regr-america

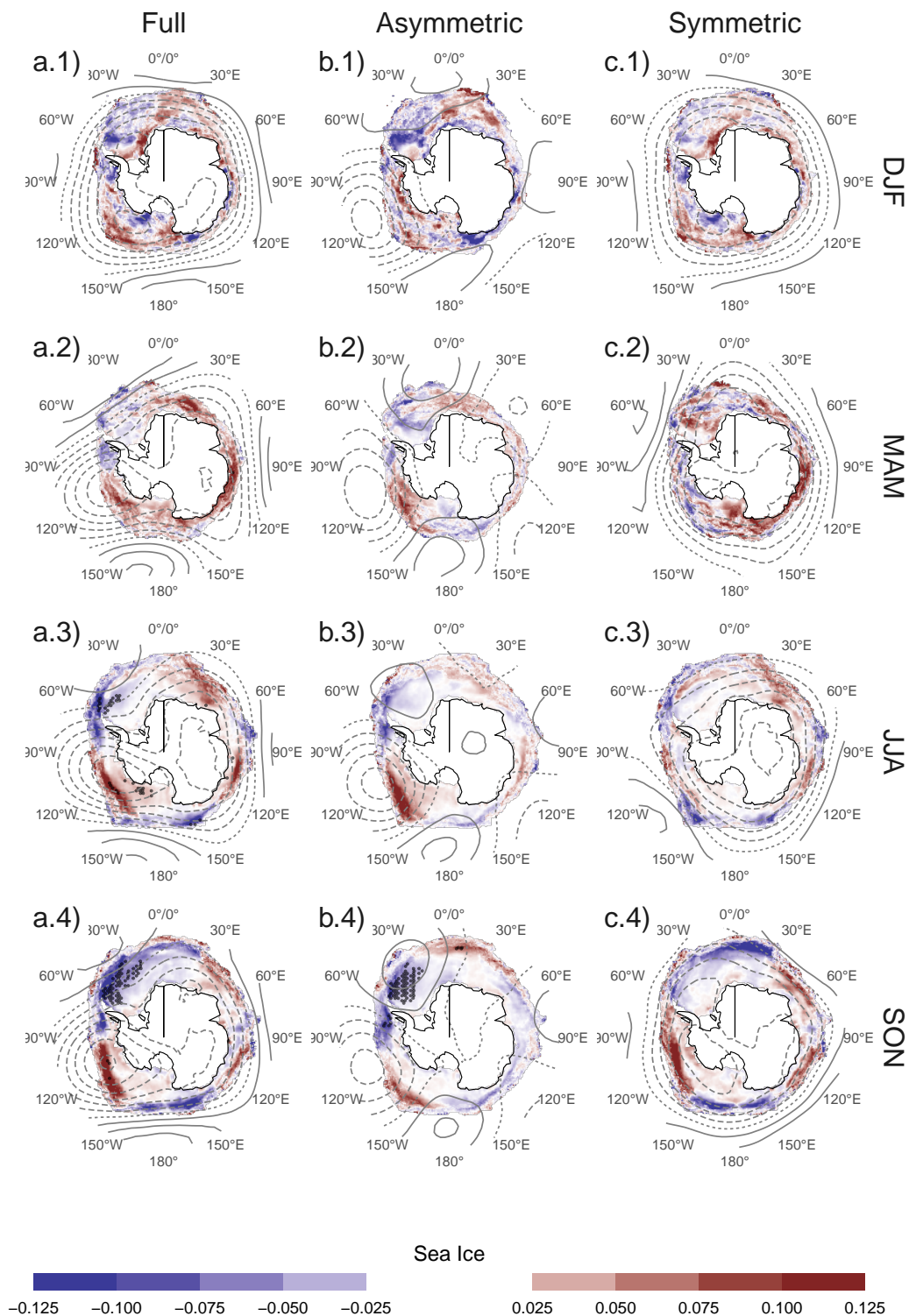


FIG. 13: Seasonal regression of SAM indices with sea ice concentration. #FIXME
fig:regr-ice

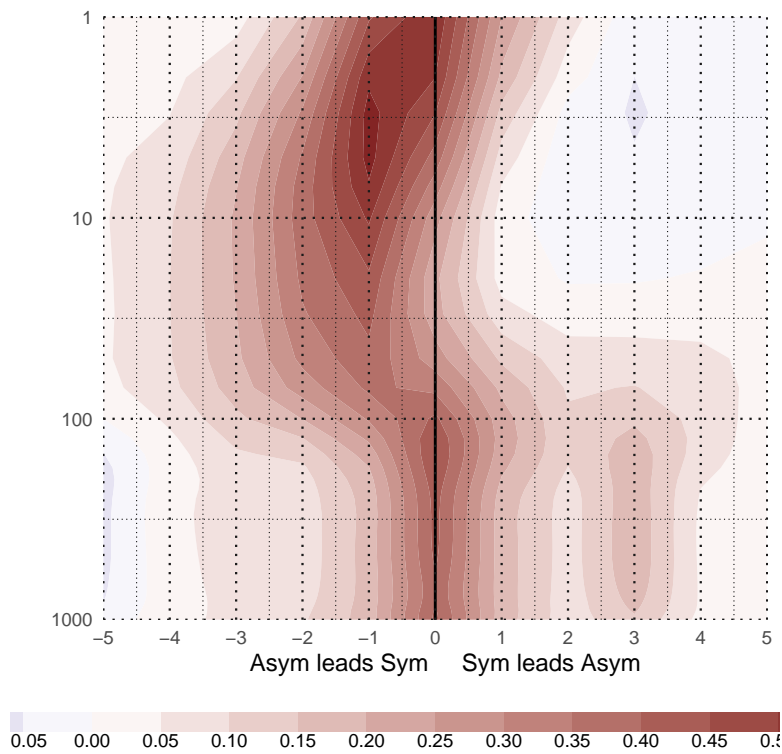


Fig. A1: Lag-correlation between Symmetric and Asymmetric SAM at each level.

fig:A1

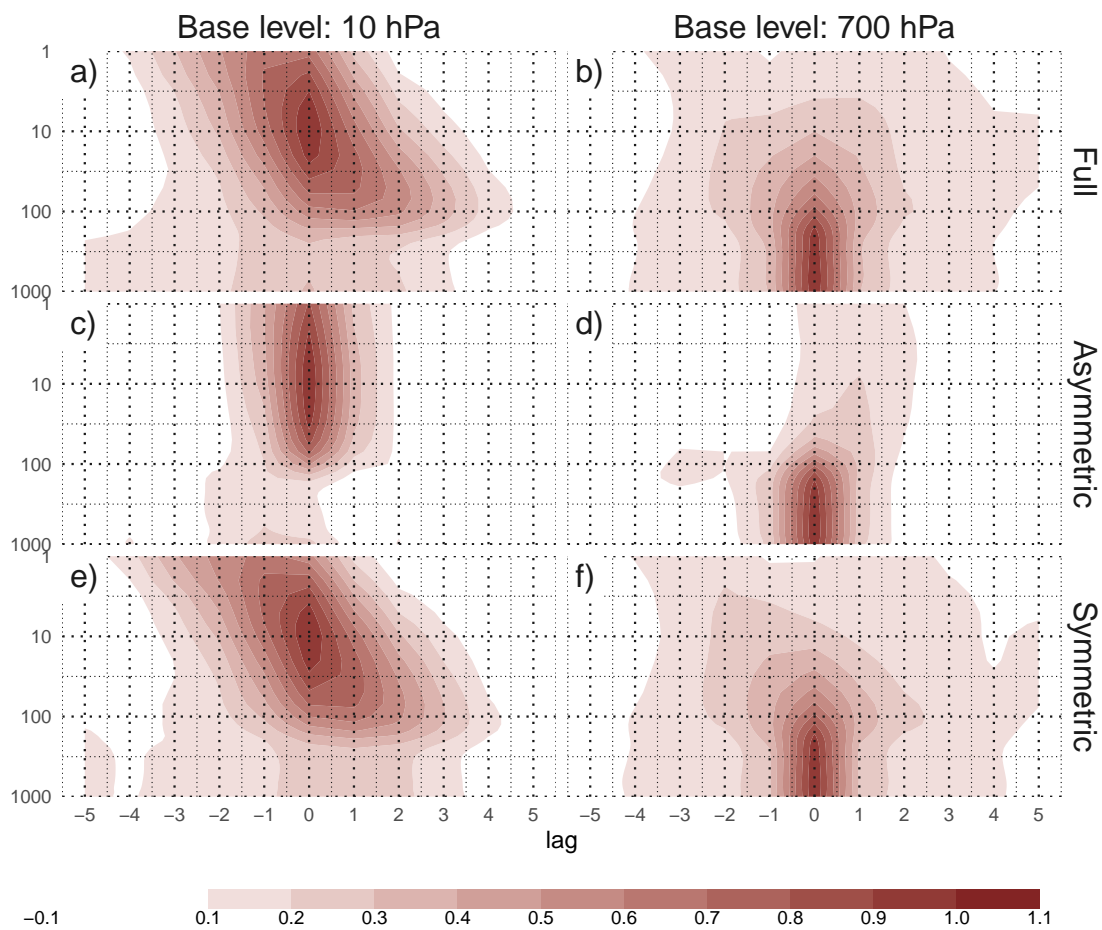


FIG. 14: Cross-correlation functions for each index and two different base levels.
fig:A2 ccf-levels

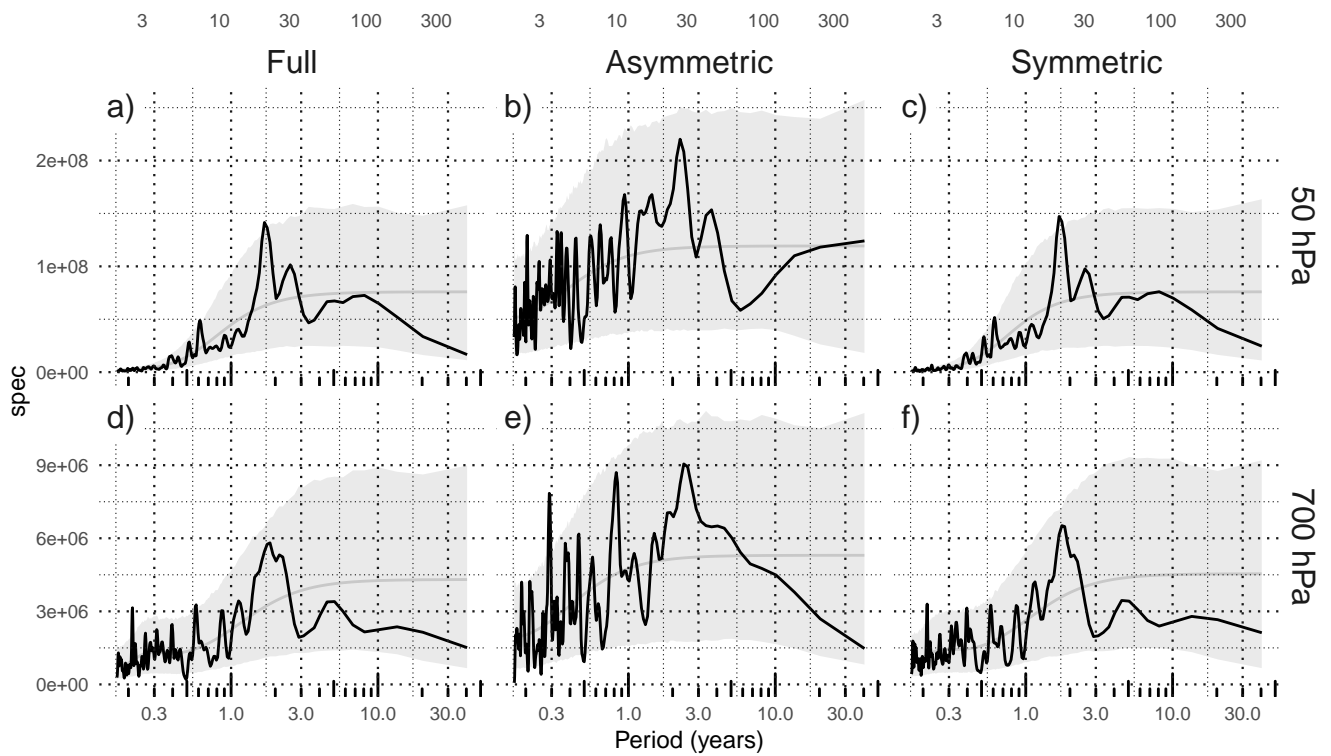


Fig. A3: Fourier spectrum of each timeseries. The shading indicates the 95% area derived by fitting an AR process to each series and bootstrapping 5000 simulated samples.

fig:A3

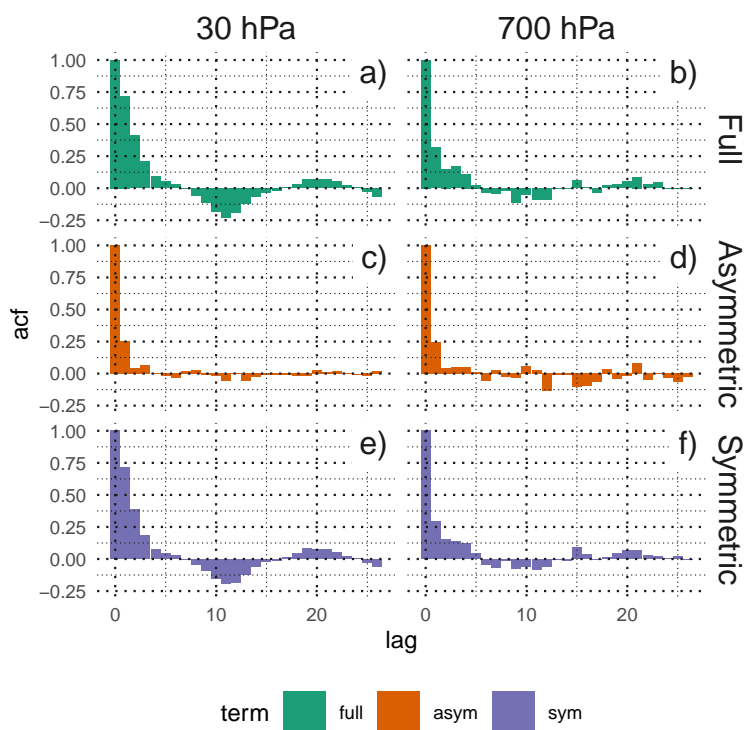


Fig. A4: Autocorrelation functions of each timeseries

fig:A4

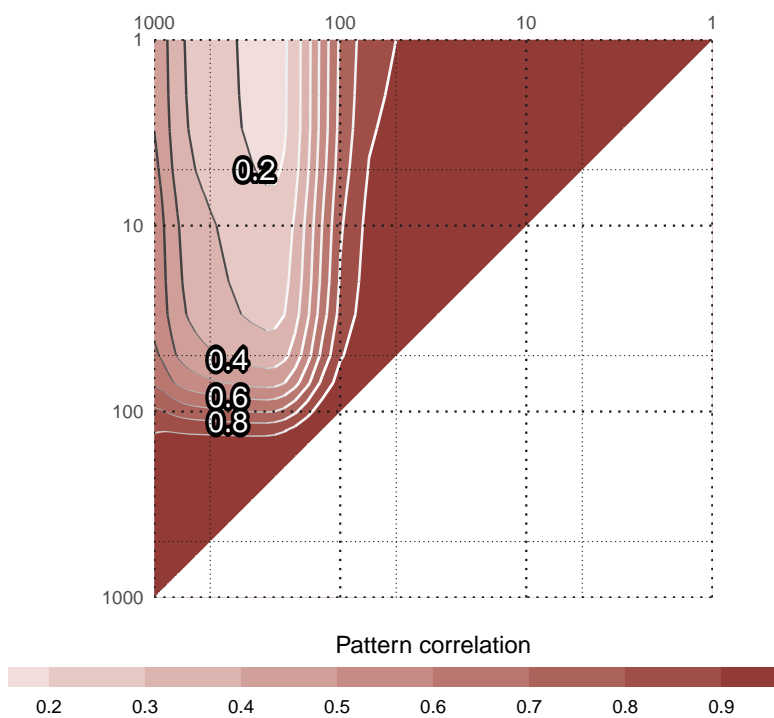


Fig. A8: Pattern cross-correlation #FIXME!

fig:A8

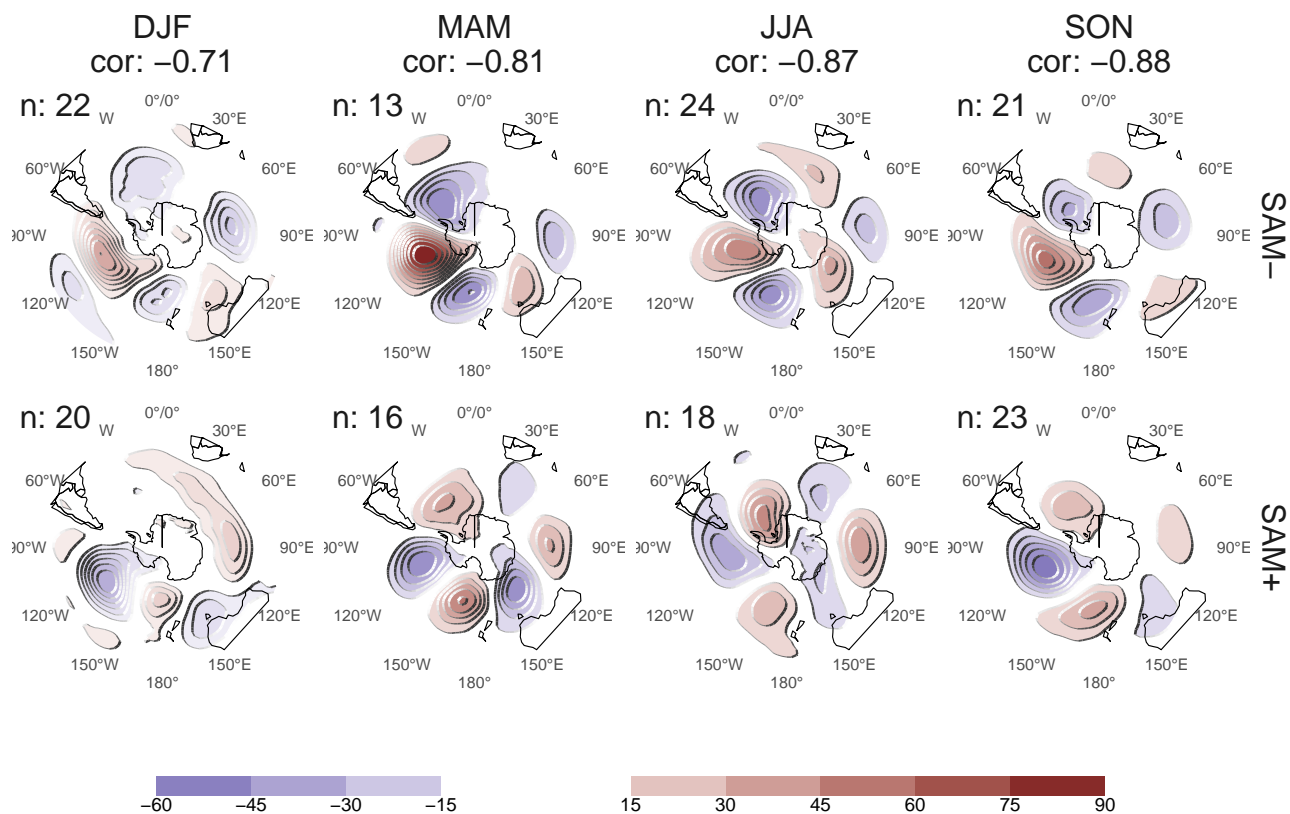


FIG. 15: 700 hPa Geopotential height zonal anomalies of composites of positive and negative SAM months selected using 1 standard deviation as threshold. Numbers in the column headers are pattern correlation between SAM+ and SAM- composites and number of monthly fields used to construct the composites.

fig:A9

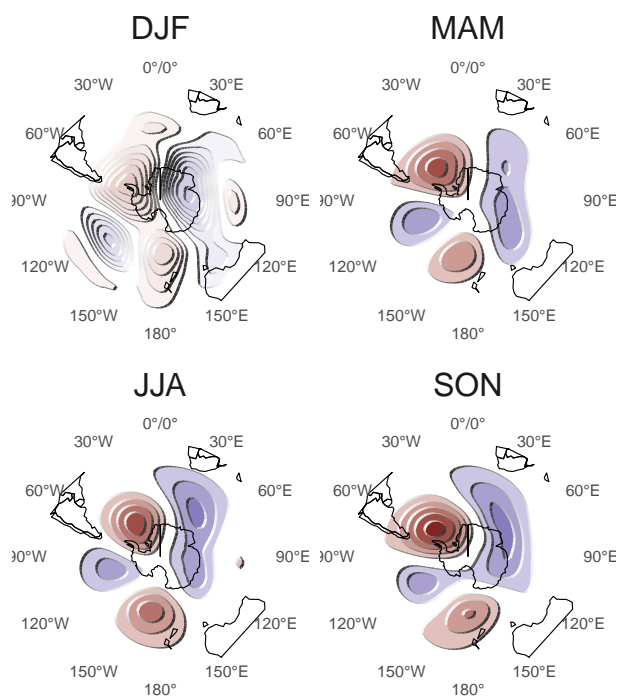


FIG. 16: Zonal of projection of 700 hPa onto the first EOF of each season.

fig:A10